

Experimental and Computational Studies to Understand Unsteady Aerodynamics of Cycloidal Rotors in Hover at Ultra-low Reynolds Numbers

Carolyn M. Walther * David A. Coleman * Moble Benedict ‡

Department of Aerospace Engineering, Texas A&M University
College Station, Texas, U.S.A.

Vinod Lakshminarayan †

Science and Technology Corporation,
Ames Research Center, Moffett Field, CA, 94035

ABSTRACT

This paper provides a fundamental understanding of the unsteady aerodynamic phenomena on a cycloidal rotor blade operating at ultra-low Reynolds numbers ($Re \sim 18,000$) by utilizing a combination of experimental (force and flowfield measurements) and computational (CFD) studies. For the first time ever, the instantaneous blade fluid dynamic forces on a rotating cyclorotor blade were measured, which, along with PIV-based flowfield measurements revealed the key fluid dynamic mechanisms acting on the blade. A 2D CFD analysis of the cycloidal rotor was developed and systematically validated using both force and flowfield measurements. Studies were performed with both static and dynamic blade pitching. Direct comparison of the static and dynamic pitch experimental results helped isolate the unsteady phenomena (such as dynamic stall, unsteady virtual camber, etc.) from the steady effects. The dynamic blade force coefficients were almost double the static ones clearly indicating the role of unsteady mechanisms on force production on cyclorotor blades. For the dynamic case, the blade lift monotonically increased even up to $\pm 45^\circ$ pitch amplitude due to dynamic stall phenomenon; however, as expected, for the static case, the flow separated from the leading edge after around 15° with large laminar separation bubble (LSB) and eventually completely separating at higher pitch angles. For both static and dynamic pitching cases, there was significant asymmetry in the lift and drag coefficients between positive and negative pitch angles due to the flow curvature effects (virtual camber). CFD flow solution and PIV measured flowfield correlated well and both showed the formation and shedding of strong dynamic stall or leading edge vortices, especially at higher pitch amplitudes, which is the reason for the stall delay and force enhancement. Also, the dynamic stall process during the upper half of the trajectory was significantly different from the lower half even with symmetric blade pitch kinematics because of the reversal of dynamic virtual camber from the upper to the lower half. Even at such low Reynolds numbers the pressure forces, as opposed to viscous forces, were found to be dominant on the cyclorotor blade. The power required for rotation (rather than pitching power) was the domineering component of the total blade power for the dynamic pitching case.

NOTATION

A	Rectangular projected rotor area	P_{ROT}	Rotational power
b	Blade span	P_{TOTAL}	Total power
AR	Aspect ratio	R	Rotor radius
c	Blade chord length	T	Thrust
C_L	Coefficient of lift	TE	Trailing edge of blade
C_D	Coefficient of drag	v_i	Induced velocity
C_{MZ}	Pitching moment coefficient	β	Angle between chord and resultant force
C_P	Power coefficient	Ω	Rotational speed of rotor
C_T	Thrust coefficient	φ	Phase angle
d	Cyclorotor diameter	Ψ	Azimuthal position of blade
D	Drag force	θ	Blade pitch angle
FM	Figure of merit	$\dot{\theta}$	Blade pitch rate
L	Lift force		
LE	Leading edge of blade		
M_Z	Pitching moment		
PIV	Particle image velocimetry		
P_{IDEAL}	Ideal power		
P_{PITCH}	Pitching power		

* Graduate Research Assistant

‡ Assistant Professor

† Research Scientist

2017 AHS Robert L. Lichten Award Winner

Presented at the AHS International 73rd Annual Forum & Technology Display, Fort Worth, Texas, USA, May 9-11, 2017. Copyright © 2017 by AHS International, Inc. All rights reserved.

INTRODUCTION

The development of efficient, maneuverable, gust tolerant, and sustained hover-capable micro air vehicle (MAV) platforms with expanded flight envelope is the key to the success of many missions in both military and civilian scenarios. During the past decade, there have been many studies on experimental optimization of MAV-scale conventional rotors (Refs. 1 and 2). These studies helped improve the hover figure of merit of a micro-rotor from an initial value of 0.42 to 0.65. However, this maximum figure of merit is still far below the full-scale helicopter value (~ 0.85) and is attributed to low Reynolds number (10^4 – 10^5) aerodynamics, especially the low airfoil lift-to-drag ratios and the complex induced wake distribution below the rotor (Ref. 2). Therefore, the vehicles developed using these optimized rotors could only achieve a maximum hover endurance of 10 minutes which would make them incapable of any realistic missions (Refs. 1 and 2). This clearly indicates the need for a step improvement in hover efficiency, which could only be achieved through a radically different concept to fly at these low Reynolds numbers. A new revolutionary concept of a cyclocopter or a cycloidal rotor based aircraft (Fig. 1) is being investigated.

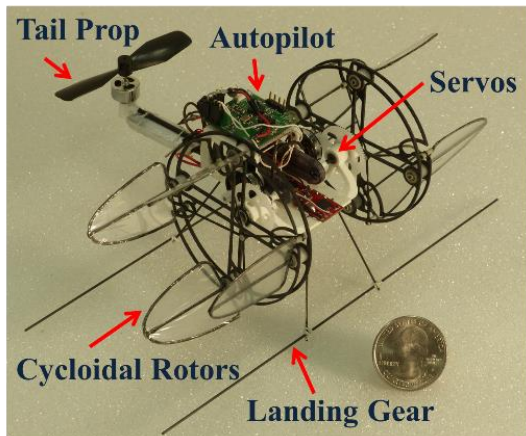


Fig. 1: 29-gram meso-scale cyclocopter.

A cycloidal rotor (or cyclocopter) is a rotating-wing system (Fig. 1) where the span of the blades runs parallel to the axis of its rotation. The pitch angle of each blade is varied cyclically by mechanical means such that each blade experiences positive geometric angles of attack at both the top and bottom halves of its circular trajectory (Fig. 2). The resulting time-varying lift and drag forces produced by each blade is resolved into the vertical and horizontal directions, as shown in Fig. 2. With this kind of cyclic blade kinematics, the blades produce a net thrust. Varying the amplitude and phase of the cyclic blade pitch is used to change the magnitude and direction of the net thrust vector produced by the cyclocopter.

Pioneering research on the cyclocopter concept for micro air vehicle (MAV) applications has been conducted over the last ten years (Ref. 3 – 15). This body of work represents one of the most comprehensive evaluations ever conducted on cyclocopters at MAV scales and involved systematic

performance measurements in both hover (Ref. 3 – 7) and in a wind tunnel (Refs. 8 – 10), flowfield studies using Particle Image Velocimetry (PIV) (Refs. 3 – 5), computational fluid dynamic (CFD) analysis (Refs. 8 and 9), and aeroelastic modeling (Ref. 11).

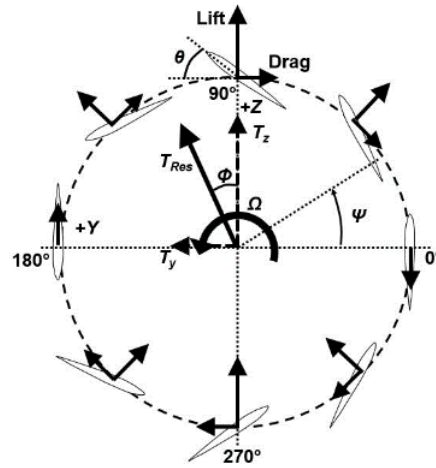


Fig. 2: Cyclocopter blade kinematics.

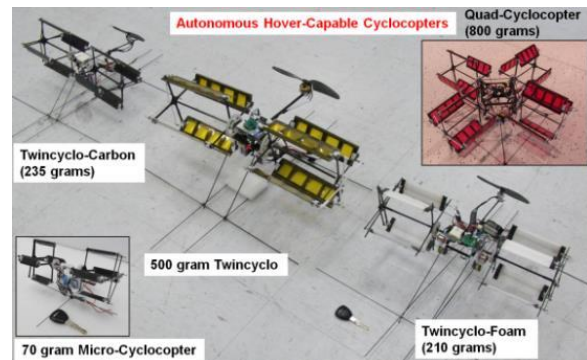


Fig. 3: Hover-capable cyclocopters developed in the past.

These studies established a fundamental understanding of the cyclocopter performance, and helped in formulating a set of design principles for an efficient cyclocopter operating at MAV-scale Reynolds numbers ($Re < 40,000$). This work, along with innovative vehicle design techniques and the development of novel autonomous flight control strategies, has led to the first flying cyclocopter-based aircraft (Ref. 12). Since then, a wide range of hover-capable cyclocopter aircraft ranging in size from 29 to 800 grams have been developed (Refs. 12 – 15), demonstrating conclusively the feasibility of the cyclocopter concept for MAV applications (Figs. 1 and 3). Based on results from these previous studies (Ref. 6), it has been shown that this concept has the potential to achieve higher levels of aerodynamic efficiency (almost 50% higher) than a conventional rotor (Fig. 4). The possible reasons for the improved performance could be the uniform spanwise load distribution on the cyclocopter blades and the favorable unsteady aerodynamic mechanisms.

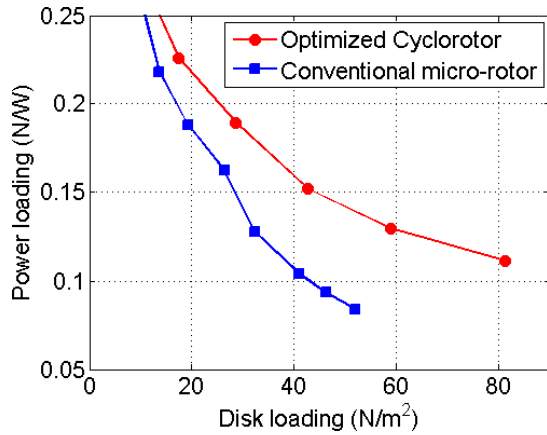


Fig. 4: Thrust/power of cyclorotor versus conventional rotor.

Systematic forward flight studies were also conducted in the wind tunnel, which showed the potential for a cyclorotor to perform efficient high-speed forward flight even beyond an advance ratio of 1.0 by a simple phasing of the cyclic blade-pitch schedule (Refs. 10 and 13). As shown in Fig. 5, the power required decreased by almost 40% from hover to an advance ratio close to unity, which is phenomenal for an MAV-scale rotor.

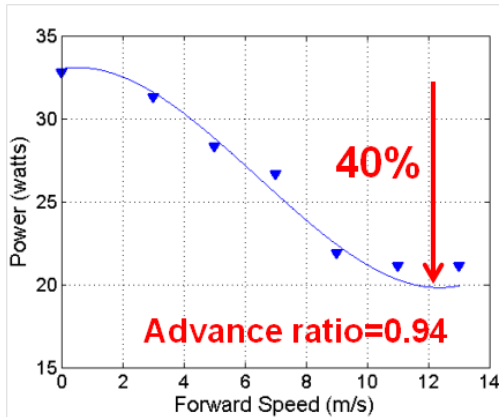


Fig. 5: Forward flight performance of a cyclorotor.

A twin-cyclocopter (Fig. 1) has 5 control degrees of freedom (three RPMs and two thrust directions) (Refs. 13). As a result, the cyclocopter would have greater actuation potential than a typically under-actuated system such as a quad-rotor. In other words, the cyclocopter can potentially command instantaneous accelerations in more directions than a quad-rotor. Another potential advantage of a cyclorotor, especially for indoor reconnaissance missions, is its lower acoustic signature when compared to conventional quad-rotors owing to the lower rotational speed. The only drawback of a cyclorotor is the rotor structural weight, which needs to be significantly reduced in the next generation of cyclocopter designs.

It is important to note that the key focus of the previous cyclorotor research was to understand the time-averaged rotor performance (lift, thrust, and power) in both hover and forward flight at moderately low Reynolds numbers ($Re \sim 40,000$) (Refs. 3 – 10). However, there is a significant dearth

in the understanding of the unsteady blade aerodynamics, which is even more important at the ultra-low Reynolds numbers at which the next generation of meso-scale cyclocopters would operate. For a meso-scale cyclocopter shown in Fig. 1 (radius = 1 inch, weight = 29 grams), the operating Reynolds number is around 18,000. At these ultra-low Reynolds numbers, the steady airfoil performance (lift/drag) would be significantly lower compared to moderately low Reynolds numbers ($Re \sim 40,000$). Additionally, the flow will be extremely susceptible to separation and therefore, even the smallest perturbation could stall conventional rotor blades. In these types of conditions, we expect the unique unsteady aerodynamics of a cyclorotor to greatly enhance performance, similar to that of a flapping wing. This means, understanding and utilizing the potential of blade unsteady aerodynamics becomes important at these extremely low Reynolds numbers. Therefore, if the focus of the previous research was on time-averaged performance, the goal of the present study is to understand unsteady blade aerodynamic loads in hover at much lower Reynolds numbers ($Re < 20,000$). Knowing the forces and flowfield at each instant of the blade trajectory can reveal key information about how the blade lift, drag and pitching moment are affected by blade pitching kinematics and unsteady flow curvature effects, which forms the motivation for the present work.

Obtaining the instantaneous unsteady forces is extremely challenging if the experiments are conducted in air because at high rotational speeds, the aerodynamic forces are corrupted by the large inertial forces. Therefore, the present study conducted at Texas A&M University utilizes a unique experimental setup to measure the instantaneous blade fluid dynamic forces and flowfield (PIV) on a hovering cyclorotor blade in water at matched Reynolds numbers. The experimental study is complemented by a 2D CFD analysis, which is systematically validated with both force and flowfield measurements. The goal of the proposed research is to measure, for the first time ever, the instantaneous blade forces on a cyclorotor blade at ultra-low Reynolds numbers ($Re \sim 18,000$) and high reduced frequencies ($k \sim 0.3$), and to utilize these results along with PIV flowfield measurements and CFD simulations to unravel the key fluid dynamic mechanisms on a cyclorotor blade.

EXPERIMENTAL METHODOLOGY

In order to gain understanding of the unsteady flow phenomena on a cyclorotor blade, the instantaneous blade forces are measured in water at matched Reynolds numbers. The reason for conducting these experiments in water is due to the ability to match the Reynolds numbers at significantly lower rotor speeds and higher fluid dynamic to inertial force ratio when compared to experiments in air. The forces are directly measured at the blade root using a miniature 6-component force balance. To obtain just the fluid dynamic forces acting on the cyclorotor blade, the following procedure is followed: first, the total forces are acquired by performing the experiment in water; next, the inertial forces are obtained

by repeating the same experiment in air; finally, to calculate the pure fluid dynamic forces, the inertial forces are subtracted from the total forces. Figure 6 shows the three forces in the radial direction as a function of blade azimuthal position. It can be seen that the inertial forces are only a small fraction of the total forces in water.

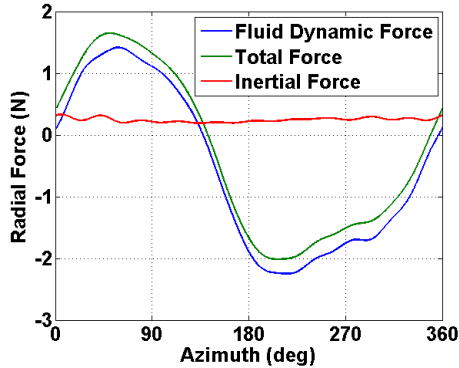


Fig. 6: Blade radial force versus azimuthal location.

Experimental Setup

The experimental setup is shown in Fig. 7. For this experiment, the forces and moments are directly measured at the blade root using a miniature 6-component force balance (ATI Mini 27 Titanium). Instead of using the conventional four-bar based blade pitching mechanism, individual blade control (IBC) is implemented using an analog feedback servo. This allows to electronically couple the blade pitch angle with its azimuthal location (obtained using an encoder) by commanding the servo to provide the required blade pitch kinematics based on the feedback from the blade azimuthal position. The electronic blade pitch control greatly simplifies the blade pitch mechanism. The cyclorotor is 1-bladed with a radius of 3.43 inches, and is rotated by a Maxon EC 22 brushless motor that is equipped with Hall-effect sensors for precise rpm control. The motor is mounted in series with a Maxon Planetary Gearhead with a reduction ratio of 370:1. A 12-channel slip ring is used to transmit the signals from the balance and servo in the rotating frame to the data acquisition equipment in the stationary frame. The tests are performed in a 3.2 ft X 1.6 ft X 2.4 ft rectangular tank, and with a rapid prototyped printed blade. The blade airfoil is a NACA 0015, and has a 12-inch span and 2-inch chord resulting in an effective aspect ratio of 12 (since there is only one free tip). The blade has been coated with shellac to seal any pores in the ABS plastic blade material resulting in water absorption that could corrupt the inertial force measurements.

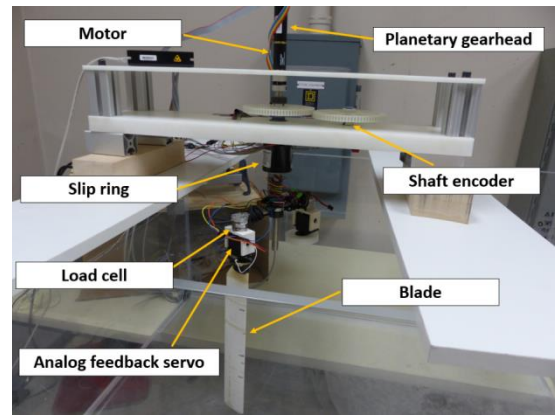


Fig. 7: Single-bladed cyclorotor test rig in water tank.

For conducting detailed flowfield measurements, the same cyclorotor test-rig is implemented with a state-of-the-art PIV system shown in Fig. 8. This system includes an EverGreen dual pulsed laser and power supply, which have been positioned next to the tank. An LaVision Imager sCMOS scientific camera with 5.5 megapixel resolution has been mounted underneath the tank, and pointed normal to the blade tip. The laser has been mounted such that the laser sheet hits midspan on the blade, which allows for visualization of mostly 2-dimensional flow (schematic of the PIV setup shown in Fig. 9). The images are captured and processed using the LaVision DaVis 8 data acquisition and visualization software.

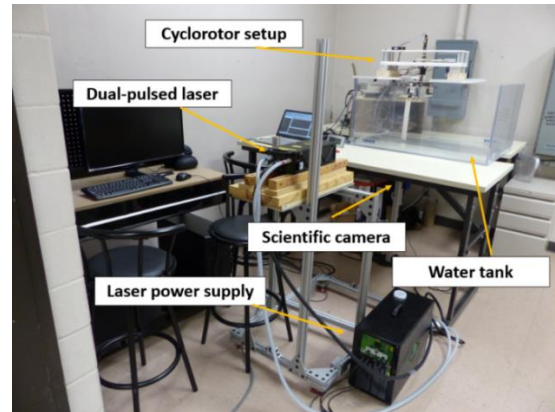


Fig. 8: PIV setup.

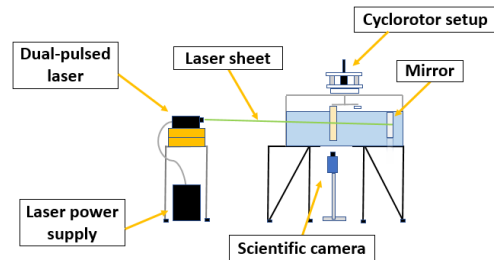


Fig. 9: Schematic of PIV setup.

Blade Force and Moment Measurements

Blade forces and moments were measured for both static and dynamic pitch cases. For the static cases, as shown in Fig. 10, the blade pitch angle with respect to the tangent of its circular trajectory was held constant. The purpose of these tests was to understand the effect of static angle of attack and steady flow curvature effects such as virtual camber (explained in subsequent sections), due to the curvilinear nature of the flow experienced by the cyclorotor blades. A static pitch angle sweep from -45° to $+45^\circ$ was performed at 40 RPM in water, which corresponds to a Reynolds number of approximately 18,000. The next step was to conduct dynamic blade pitch experiments on the cyclorotor, meaning that the blade was actively pitched using the blade pitch servo to replicate the cyclic blade pitching kinematics shown in Fig. 2. A pitching amplitude sweep from $\pm 5^\circ$ to $\pm 45^\circ$ in steps of 5° was tested at 40 RPM similar to the static case. For each test case, data was recorded for 3 minutes: about 20 seconds of tare data (rotor not rotating), 2 minutes of rotor operating at desired RPM, and the rest of the time duration was used for increasing and decreasing the rotor speed. The data was then processed and analyzed using MATLAB. Each time-history curve presented in the paper is an average of 80 waveforms (from 80 consecutive cycles after the rotor has reached the steady state).

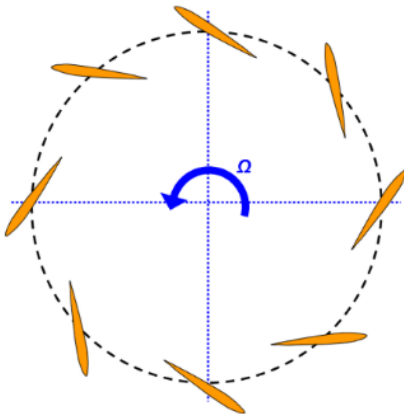


Fig. 10: Blade kinematics for static pitch case.

The purpose of doing both static and dynamic pitch experiments was to compare the measured blade forces and flowfield from the two cases and then isolate the unsteady aerodynamic force production mechanisms from the steady ones especially in a curvilinear flow environment, which will be discussed more in the subsequent sections. In the paper, blade radial force, tangential force and pitching moment are presented. Radial force will be referred to as lift and tangential force as drag. The reason for such a terminology is the fact that the inflow velocity is much smaller than the blade speed due to very low disk loading and therefore, the radial force and lift would be approximately in the same direction.

PIV Flowfield Measurements

As mentioned before, the cyclorotor test-rig has been instrumented with a state-of-the-art PIV system, which is used

to conduct high resolution flowfield measurements around the blade. The water in the tank is seeded with $\sim 10 \mu\text{m}$ diameter glass beads. When the laser sheet hits the glass particles, the light is reflected and illuminates the flow. A mirror is also mounted at the back of the tank to reflect the laser light onto the backside of the blade so that the blade shadow is diminished (Fig. 9).

PIV measurements were performed at a rotor speed of 40 RPM for static pitch cases of 15° , 30° and 45° and dynamic pitch cases with amplitudes of $\pm 15^\circ$, $\pm 30^\circ$ and $\pm 45^\circ$ to correlate with the force and moment measurement experiments. Phase-locked PIV measurements were conducted around the blade, when the blade reached different azimuthal locations. Azimuthal resolution for the PIV measurements was 10° , which means flowfield measurements around the blade were made at 36 azimuthal locations in one rotor revolution. The size of the interrogation window around the blade was 80 mm X 66 mm. For each azimuthal location (or phase), 70 phase-locked images of the flowfield were taken at a rate of 2/3 Hz (same as the rotational speed); therefore, one image was taken per rotation. These images were processed using the LaVision DaVis 8 data acquisition and visualization software. An average of the 70 images was computed, and a velocity component representing the rotational velocity (ΩR) of 0.365 m/s was subtracted, so that the resulting flow vectors are in the rotating frame (as seen by the blade). This is how the flowfield is presented in the paper.

COMPUTATIONAL METHODOLOGY

Two-dimensional Computational Fluid Dynamic (2D CFD) simulations of the cyclorotor were performed using a Reynolds-averaged Navier–Stokes (RANS) solver called OVERTURNS (Ref. 16). This overset structured mesh solver uses the diagonal form of the implicit approximate factorization method (Ref. 17) with a preconditioned dual time scheme to solve the compressible RANS equations. Computations were performed in the body frame in a time-accurate manner. A third-order MUSCL scheme (Ref. 18) with Roe flux difference splitting (Ref. 19) and Koren’s limiter (Ref. 20) was used to compute the inviscid terms, and second-order central differencing was used for the viscous terms. Due to the low operating Mach numbers of the present cyclorotor, the inclusion of a low Mach preconditioner based on Turkel’s method (Ref. 21) helped accelerate convergence and ensure accuracy of the solution. The Spalart–Allmaras (SA) turbulence model (Ref. 22) was employed for RANS closure. This one-equation model is considered advantageous for its ease of implementation, numerical stability, and computational efficiency.

CFD simulations were performed for the static pitch as well as the dynamic pitch cases. The output included radial and tangential force predictions, which were compared with the force and moment measurements, and the flowfield solution, which was compared with the PIV-measured flowfield. The comparison was used to provide insight into the blade loads and flow phenomena around the rotor’s azimuth.

DYNAMIC VIRTUAL CAMBER

Before the results of the study are presented, a unique phenomenon known as dynamic virtual camber needs to be discussed. The virtual camber effect occurs due to the chord-wise variation of the incident velocity angle (or angle of attack) on the airfoil. This effect is very predominant in cyclorotors because the flow over a cyclorotor blade is characterized by a pitching airfoil in a curvilinear flow in the presence of inflow that varies along with azimuth. An airfoil in a curvilinear flow experiences different flow velocity magnitude and direction along the chord due to geometry and the curvilinear nature of the flow; this manifests as an effective camber and incidence. Figure 11 shows how curvilinear flow geometry creates a negative virtual camber effect for a blade at 0° pitch angle. Therefore, a symmetric blade immersed in a curvilinear flow will behave like a cambered blade in a rectilinear flow as shown in Fig. 11. This phenomenon is more significant for cyclorotors with a large chord-to-radius ratio (c/R).

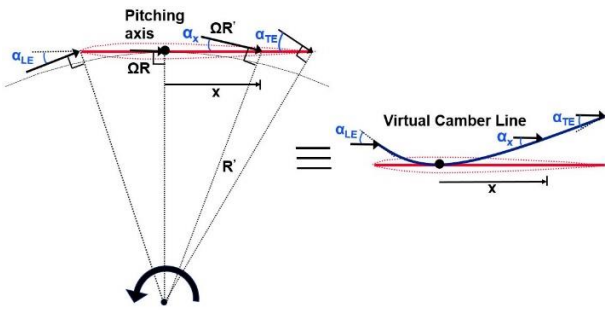


Fig. 11: Negative virtual camber effect due to curvilinear flow.

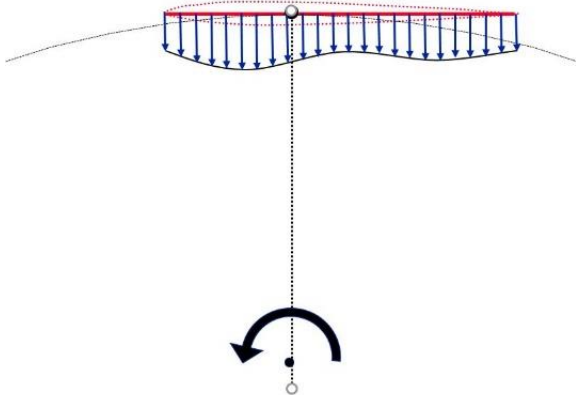


Fig. 12: Chord-wise variation of incidence due to inflow distribution.

Flow over a cyclorotor is not purely curvilinear when it is producing thrust because of the induced flow velocity, which also effects virtual camber and incidence (Fig. 12). Additionally, the blade pitch angle and pitch rate also affect the chord-wise velocity distribution and therefore, virtual camber. Figure 13 shows pitch rate causing chord-wise variation of virtual incidence which is manifested as a positive virtual camber effect. An opposite pitch rate (nose-down pitch) causes a negative virtual camber effect.

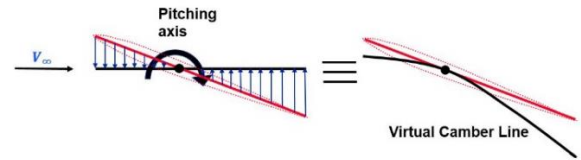
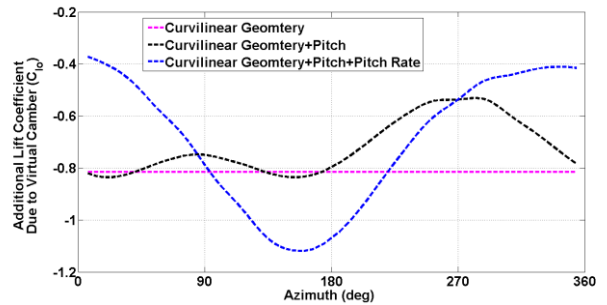
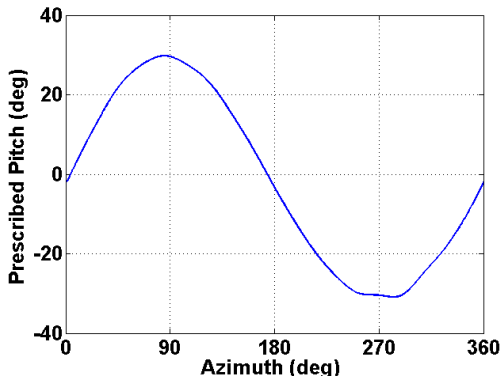


Fig. 13: Positive virtual camber effect due to pitch rate.

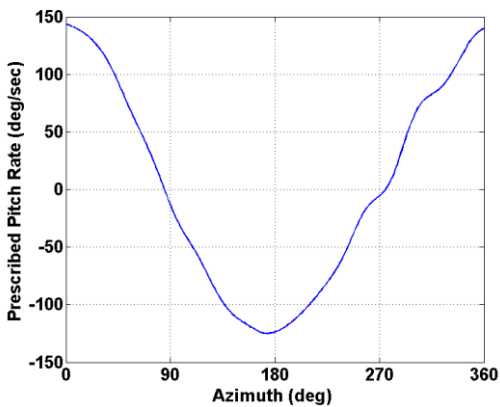
Since blade pitch and pitch rate changes with azimuthal location, corresponding virtual camber also changes with azimuth making it 'dynamic' virtual camber. In essence, the virtual camber experienced by the cyclorotor is a function of chord/radius, blade pitch angle, pitch rate and inflow. Note that on the cyclorotor blade the virtual camber would be apparent in the blade forces as additional lift. Considering all these effects, we have derived a generalized expression (discussed in detail in Ref. 23) to obtain not only the virtually cambered shape of the airfoil but also the additional lift. Figure 14 (a) shows the variation of this additional lift coefficient due to virtual camber versus azimuthal position for a cyclorotor rotating at 40 rpm with 30° pitch amplitude and Figs. 14 (b) and (c) show the corresponding prescribed pitch and pitch rate respectively, as blade goes through various azimuthal locations. Figure 14 (a-c) shows the effects of virtual camber due to several underlying physical phenomena. It can be observed that virtual camber effect due to only curvilinear geometry (or flow curvature) is static in nature (magenta line) and it always causes negative virtual camber. Pitch and pitch rate create time-dependency of virtual camber effect making it a dynamic virtual camber. Figure 14 reveals an important result that pitch and especially pitch rate creates a very dominant and characteristic virtual camber effect.



(a) Variation of additional lift coefficient due to virtual camber.



(b) Prescribed pitch along azimuth.



(c) Prescribed pitch rate along azimuth.

Fig. 14: Effect of curvilinear flow, pitch and pitch rate on virtual camber.

Figure 14 (a) shows that blade pitch (black line) decreases negative virtual camber and opposes the effects of curvilinear geometry. The effect of blade pitch is more prominent near 90° and 270° azimuth since pitch angle reaches at its peak at those locations (Fig. 14 (b)). It is also observed that pitch rate (blue line) creates positive virtual camber effect near 0° azimuth, which almost nullifies the effects of curvilinear geometry; while at 180° , it creates negative virtual camber which together with curvilinear effect produces even larger negative lift. For this reason, it will be shown later in the paper that the net lift coefficient is very small at 0° azimuth, while it is much below zero at 180° azimuth, although pitch angle is near 0° at both azimuth locations (Fig. 14 (b)). Pitch rate effect on virtual camber is dominant at 0° and 180° azimuth because pitch rate reaches its peak near these two locations (Fig. 14 (b)). Figure 15 shows graphically how pitch rate is creating opposite virtual camber effects at different azimuth locations.

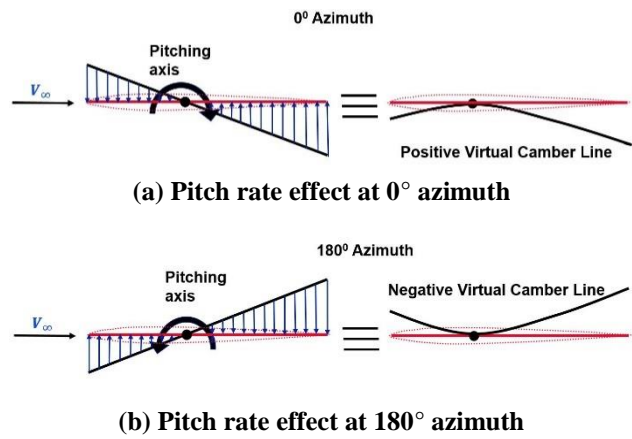


Fig. 15: Effect of pitch rate on dynamic virtual camber at two extreme azimuth locations (0° and 180°).

This phenomenon is clearly observed in Fig. 16, which shows the actual chord-line of cyclorotor blade and virtual chord-line due to virtual camber effect along different azimuth positions. It can be observed again at 0° azimuth, virtual camber is minimum producing almost negligible negative lift while at 180° azimuth it has huge negative virtual camber producing large negative lift. Based on the convention followed in the paper, lift force directed radially inwards is negative lift. The discussion section of the paper would utilize the virtual shape along with the physical airfoil to understand the physics of force production.

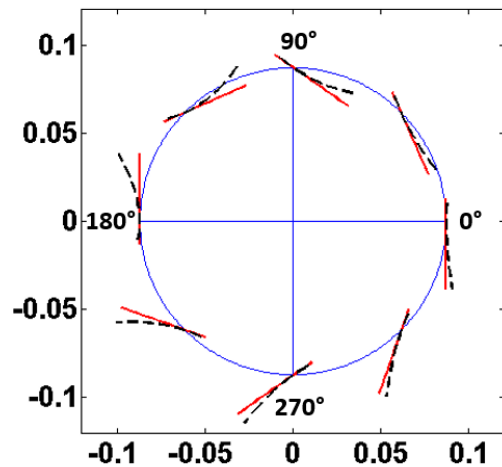


Fig. 16: Virtual chord-line due to virtual camber effect along azimuth.

COMPARISON OF EXPERIMENT AND CFD

Force Comparison (Experiment versus CFD)

The first step was to compare the CFD predicted forces with experimental data for both static and dynamic pitch cases.

Static Pitch Case: Figure 17 shows the measured lift coefficient as a function of static pitch angle plotted along

with CFD results obtained from the 2D unsteady RANS (Reynolds Averaged Navier Stokes) simulation. There is good correlation between CFD predicted lift and experimental data especially at positive angles of attack. A key observation from Fig. 17 is that lift curve is highly asymmetric between positive and negative pitch angles even though the airfoil is symmetric. A 0° pitch angle produces a non-zero lift force ($C_L = -0.75$) towards the center of the rotor because of the virtual camber effect (refer Fig. 11) explained in the previous section. Both experiment and CFD is able to capture this effect even though CFD slightly over-predicts the lift due to virtual camber.

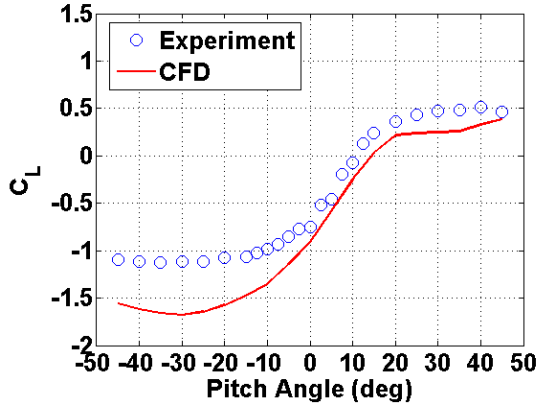


Fig. 17: Lift coefficient versus fixed pitch angle from experiment and CFD.

Note that, as shown in Fig. 16, the blade experiences reverse or negative virtual camber for the positive pitch angles and positive camber for the negative pitch angles. This manifests itself in the significantly lower magnitude of lift (max $C_L = 0.5$) for positive pitch when compared to the negative pitch (max $C_L = -1.25$) despite the nature of the symmetric airfoil.

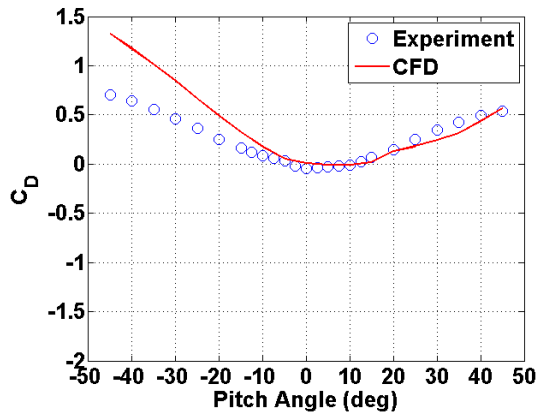
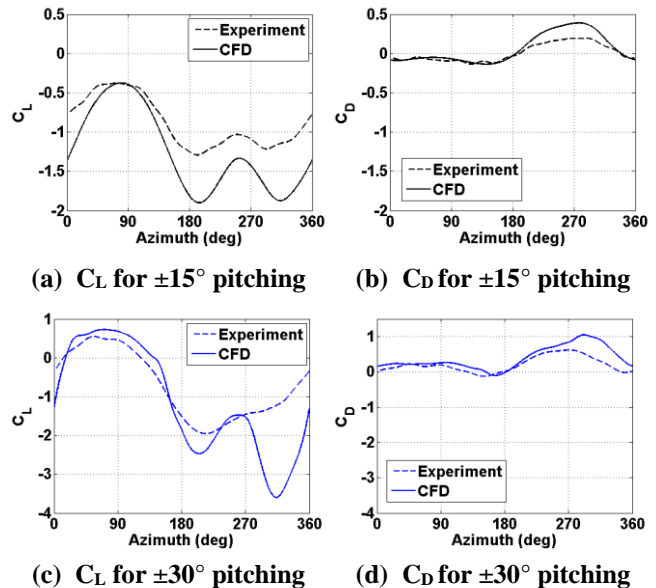


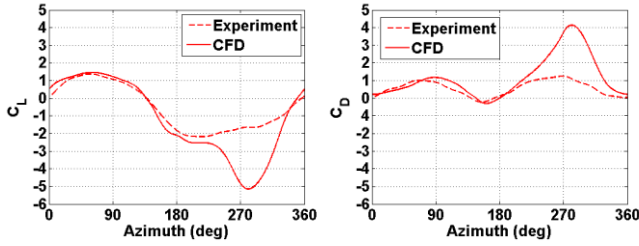
Fig. 18: Drag coefficient versus fixed pitch angle from experiment and CFD.

The drag coefficient as a function of static pitch angle is shown in Fig. 18. As before, the experimental results are plotted along with the CFD prediction and there is a good correlation between the both, especially for positive pitch angles as in the case of lift. The asymmetry in drag between the positive and negative pitch angles (negative pitch angle

causing more drag than positive ones) is due to the virtual camber effect. The CFD results show the same trend as experimental data. The maximum drag produced is larger for negative pitch angles ($C_D = 0.75$) than for positive pitch angles ($C_D = 0.6$). These results clearly show the role of virtual camber effect on the lift and drag production on a static blade experiencing a curvilinear flow. Additionally, these results are also very relevant to a fixed-pitch vertical axis wind turbine blade.

Dynamic Pitch Case: The measured and CFD predicted lift and drag coefficients as a function of azimuthal location for dynamic pitching angles of $\pm 15^\circ$, $\pm 30^\circ$, and $\pm 45^\circ$ are shown in Figure 19. For all the three cases the CFD results correlate well with the experimental data for the upper half of the azimuth ($\Psi = 0^\circ - 180^\circ$); however, CFD over-predicts both lift and drag in the lower half ($\Psi = 180^\circ - 360^\circ$). The reasons for this are not fully understood yet; however, it may be due to 3D effects which are not captured in the 2D CFD simulation. It can be seen from Fig. 19 that as expected, as the pitching amplitude increases, both the lift and drag coefficients also increase. Similar to the static pitch experimental results, there is lift asymmetry between the upper and lower halves of the azimuth for the dynamic case. The reason for this asymmetry even though the pitch kinematics is identical in the upper and lower halves (only the sign is different) can be attributed to the dynamic virtual camber effect. As shown in Fig. 16, in the upper half, the blade experiences a negative camber and hence smaller lift compared to the lower half, where the blade experiences a positive camber. As explained before, on a pitching blade the virtual camber is dynamic in nature and arises predominantly because of two reasons: (1) finite chord/radius ratio and the curvilinear nature of the flow, and also (2) the pitch-rate. Along with the blade pitch angle the dynamic camber plays a key role in the force production on a cyclorotor blade. The subsequent sections would utilize both the measured instantaneous blade forces and flowfield to understand the role of pitch angle and camber on force production on a cyclorotor blade.





(e) C_L for $\pm 45^\circ$ pitching (f) C_D for $\pm 45^\circ$ pitching

Fig. 19: Lift and drag coefficients versus azimuth for $\pm 15^\circ$, $\pm 30^\circ$, and $\pm 45^\circ$ dynamic pitching.

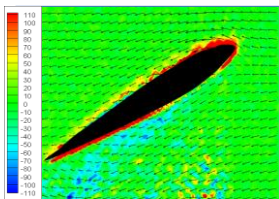
Flowfield Comparison (PIV versus CFD)

The next step was to compare the CFD predicted flowfield around the blade at different azimuthal locations with the PIV measured flowfield.

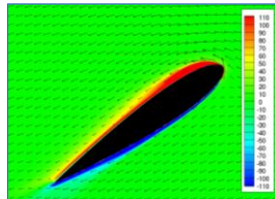
Dynamic Pitch Comparison: Figure 20 shows a comparison of flow velocity vectors and vorticity contours obtained using PIV with the flow solution predicted by CFD for the dynamic pitching case with an amplitude of $\pm 45^\circ$. The images correspond to azimuthal locations of 50° , 60° , 70° , 80° , 90° , 100° , 260° , and 270° . These azimuthal values were chosen because these are the locations where the blade attains high pitch angles and hence leads to significant growth and shedding of dynamic stall vortices. From Fig. 20, it is significant to note that, overall, there is very good correlation between PIV measured flowfield and CFD even for such high pitch amplitudes ($\pm 45^\circ$). When the blade is operating in the upper half of its circular trajectory (shown in Figs. 20 (a) – (l)), there is the formation and shedding of a strong dynamic stall or leading edge vortex (LEV). The azimuthal location of the blade is shown on the schematic in each PIV figure. As the blade pitch angle increases, the vortex increases in size. At $\Psi = 100^\circ$ (Fig. 20 (k) and (l)), the vortex begins to separate from the leading edge and convect over the blade. As the vortex disturbance moves along the chord there is an increase in the nose-down pitching moment, which is due to the aft moving center of pressure.

PIV

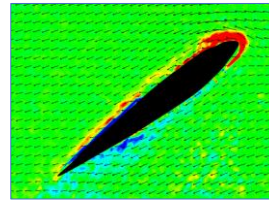
CFD



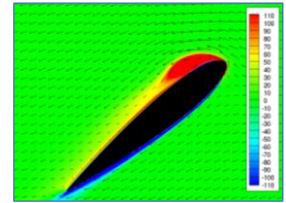
(a) $\Psi = 50^\circ$ for PIV



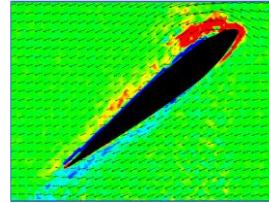
(b) $\Psi = 50^\circ$ for CFD



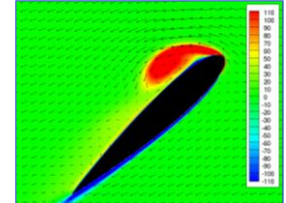
(c) $\Psi = 60^\circ$ for PIV



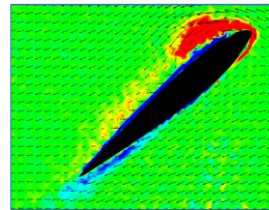
(d) $\Psi = 60^\circ$ for CFD



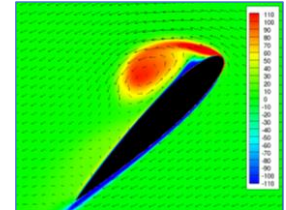
(e) $\Psi = 70^\circ$ for PIV



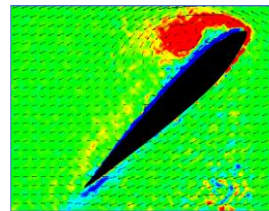
(f) $\Psi = 70^\circ$ for CFD



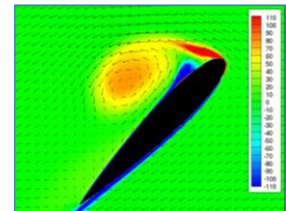
(g) $\Psi = 80^\circ$ for PIV



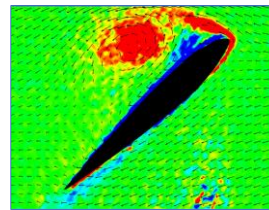
(h) $\Psi = 80^\circ$ for CFD



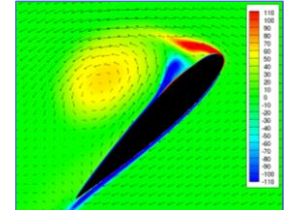
(i) $\Psi = 90^\circ$ for PIV



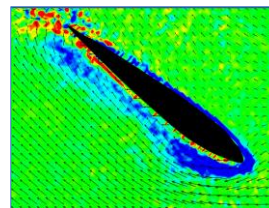
(j) $\Psi = 90^\circ$ for CFD



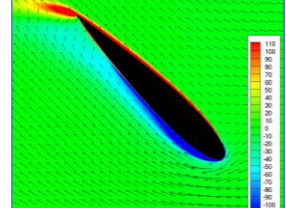
(k) $\Psi = 100^\circ$ for PIV



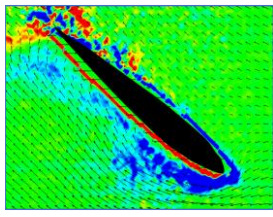
(l) $\Psi = 100^\circ$ for CFD



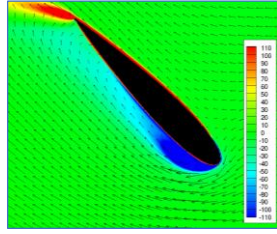
(m) $\Psi = 260^\circ$ for PIV



(n) $\Psi = 260^\circ$ for CFD



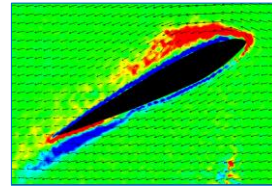
(o) $\Psi = 270^\circ$ for PIV



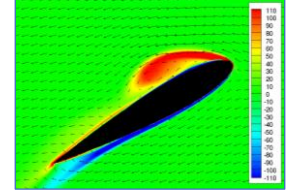
(p) $\Psi = 270^\circ$ for CFD

Fig. 20: PIV versus CFD flowfield for $\pm 45^\circ$ pitching.

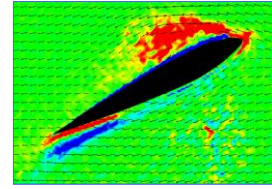
Figures 20 (m) – (o) show the blade in the lower half of the trajectory where the blade is pitched in the opposite direction (as seen by an observer in the rotating frame). In the lower half, the correlation between PIV and CFD is not as good as the upper half. As expected, the differences between the measured and predicted forces (Fig. 19) in the lower half will also manifest in the flowfield. However, overall flowfield comparison seems good. Even in the lower half, it can be seen from both the CFD and PIV images that a similar vortex disturbance is building up on the leading edge. The colors of the vortex here (fuscha and blue) are different from those of the vortex on the upper half of the cycle (red and orange) due to the change in the sign of the vorticity. The rolling-up of the shear layer has switched directions which results in vorticity of opposite sense and hence, opposite sign. It is also important to note that, even though the blade is symmetric, the flow phenomena during the nose-up and nose-down pitching is very dissimilar primarily because of the dynamic virtual camber, which is in opposite direction for nose-up and nose-down pitching because of the fact that the flow curvature is always in one direction (refer to Fig. 16).



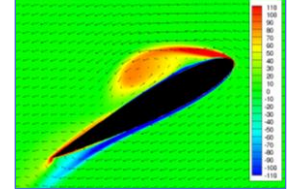
e) $\Psi = 100^\circ$ for PIV



f) $\Psi = 100^\circ$ for CFD



g) $\Psi = 110^\circ$ for PIV



h) $\Psi = 110^\circ$ for CFD

Fig. 21: PIV versus CFD flowfield for $\pm 30^\circ$ pitching

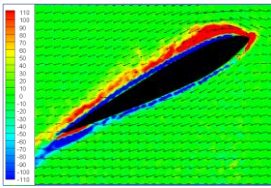
The PIV and CFD flowfield comparison for the dynamic pitching case for an amplitude of $\pm 30^\circ$ is shown in Fig. 21. The images correspond to azimuthal locations of 80° , 90° , 100° , and 110° . Again in this case there is very good correlation between CFD and PIV measured flowfield, which is notable considering the complexity in the flowfield. As in the $\pm 45^\circ$ dynamic pitching case, a vortex disturbance is seen building on the leading edge in images from 21 (a) – (d). It should be noted that the dynamic stall vortex for the $\pm 30^\circ$ case does not reach the strength nor develop the same way as the vortex in the $\pm 45^\circ$ case. For example, at the azimuthal location of 90° , the $\pm 45^\circ$ case (Fig. 20 (i) and (j)) shows a vortex that is just starting to separate from the leading edge, whereas the $\pm 30^\circ$ case for the same azimuthal location (Fig. 21 (c) and (d)), shows a vortex that is still building up at the leading edge. Dynamic stall in a curvilinear flow, especially, at such high pitch amplitudes have never been investigated before at any scales. This finding is not intuitive because one would expect the blade to be fully stalled at a pitch angle of 30° and the flow to just separate from the leading edge. However, due to the unique unsteady flow mechanisms at ultra-low Reynolds numbers in a dynamic pitching environment, the flow remains more or less attached with a strong leading edge vortex even when the blade pitch angle reaches 30° (Fig. 21 (c) and (d)) greatly enhancing the lift coefficient as shown in Fig. 19.

DYNAMIC PITCHING EXPERIMENTAL RESULTS

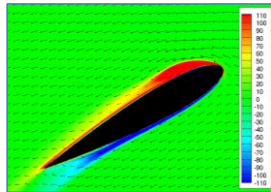
The force and moment results from the dynamic blade pitch experiments are shown in Figs. 22 – 25. The measured blade pitch angle and lift coefficient as a function of the azimuth for a pitching amplitude sweep of $\pm 5^\circ$ to $\pm 45^\circ$ are shown in Figs. 22 and 23, respectively. Similar to the static experiments lift asymmetry can be seen between upper (0° - 180°) and lower (180° - 360°) halves (Fig. 23) due to the virtual camber effect. As shown in Fig. 16, the blade pitch is positive in the upper

PIV

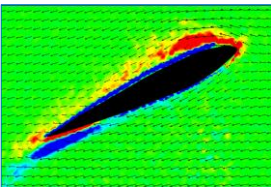
CFD



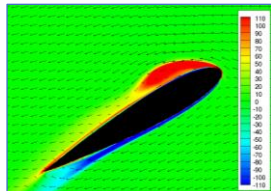
a) $\Psi = 80^\circ$ for PIV



b) $\Psi = 80^\circ$ for CFD



c) $\Psi = 90^\circ$ for PIV



d) $\Psi = 90^\circ$ for CFD

half resulting in reverse or negative virtual camber and hence smaller lift compared to the lower half where the camber is positive (due to negative pitch). The most significant finding from these results is the large values of the dynamic lift coefficients shown in Fig. 23 when compared to the static lift values shown Fig. 17. The maximum static C_L value for positive pitch is around 0.5 (Fig. 17); whereas the maximum dynamic C_L value for positive pitch is around 1.25 ($\pm 45^\circ$ pitching case), which is more than double. The same effect happens for negative pitch where the maximum static C_L is around -1.2 (Fig. 17), whereas the maximum dynamic C_L during negative pitch is around -2 ($\pm 45^\circ$ pitching case). It is significant to note that the lift coefficient monotonically increases all the way up to a pitching amplitude of $\pm 45^\circ$, which, as mentioned previously, is not intuitive because one would expect the blade to stall completely at amplitudes much lower than 45° .

The measured drag coefficient as a function of azimuth for the same pitch amplitudes is plotted in Fig. 24. Even the drag coefficient is asymmetric between the upper and lower halves and magnitude is significantly higher than the static cases shown in Fig. 18. To understand the reason for this huge increase in dynamic lift and drag coefficients on a pitching blade as opposed to a static blade in a curvilinear flow, it is important to look at the flowfield around the blade at different azimuthal locations, which is presented in the subsequent sections.

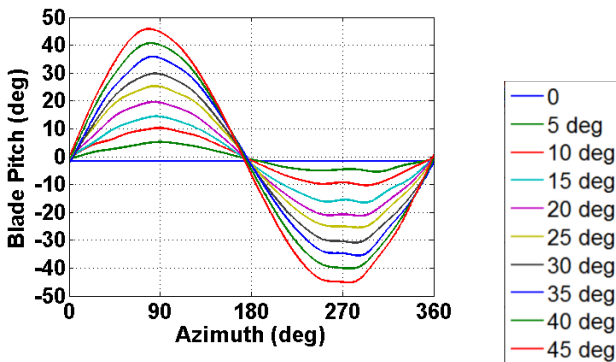


Fig. 22: Measured blade pitch versus azimuth for $\pm 0^\circ$ to $\pm 45^\circ$ dynamic pitching.

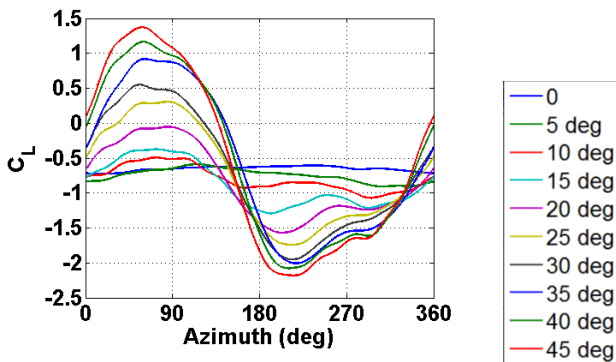


Fig. 23: Measured lift coefficient versus azimuth for $\pm 0^\circ$ to $\pm 45^\circ$ dynamic pitching.

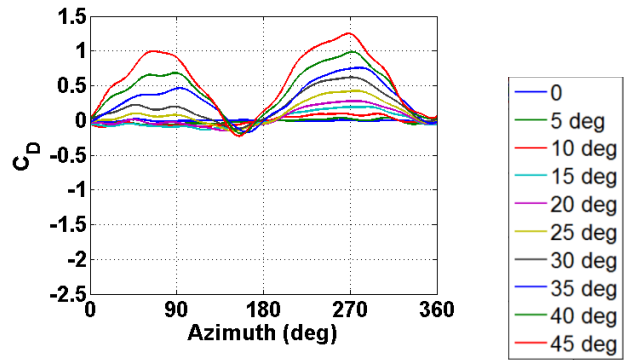


Fig. 24: Measured drag coefficient versus azimuth for $\pm 0^\circ$ to $\pm 45^\circ$ dynamic pitching.

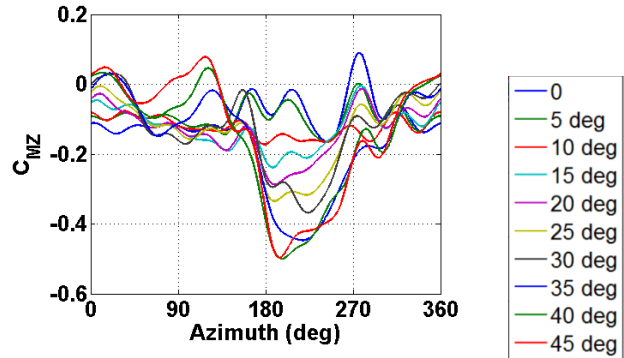


Fig. 25: Measured pitching moment coefficient versus azimuth for $\pm 0^\circ$ to $\pm 45^\circ$ dynamic pitching.

Figure 25 shows the variation of the pitching moment coefficient as a function of the azimuth. As mentioned previously, as the blade pitches nose-up and -down, the dynamic-stall vortex is swept downstream and the center of pressure shifts along the chord. This causes a large nose-down pitching moment on the blade. From Fig. 25 it can be seen that the blade experiences moment stall at azimuthal locations of approximately 120° in the upper half and in the lower half at approximately 190° . From the flowfield measurements it can be seen that the local maximum in the upper half is indicative of moment stall due to the formation of a spilled vortex and the local maximum in the lower half occurs during a state of full separation.

To better understand the source of lift and drag forces on a cyclorotor blade operating at ultra-low Reynolds numbers ($Re \sim 18,000$), it is helpful to identify whether the dominating forces are due to pressure or viscous forces. If there are only pressure forces, the resultant force (denoted by R in Fig. 26) would be normal to the blade chord. In Fig. 26, β represents the angle between the resultant of the lift and drag forces (R) and blade chord. If the forces are indeed dominated by the pressure force, R would be more or less normal to the chord and β would be close to 90° .

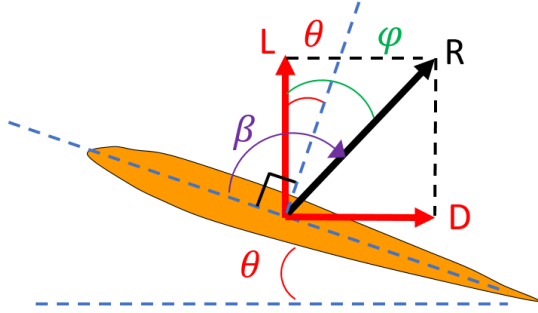


Fig. 26: Schematic showing blade forces.

The lift and drag shown in the diagram can be defined as:

$$L = R \cos \varphi \quad (\text{Eq 1})$$

$$D = R \sin \varphi \quad (\text{Eq 2})$$

where φ , the phase angle between the lift vector and the resultant vector is the following:

$$\varphi = \tan^{-1}(D/L) \quad (\text{Eq 3})$$

Finally, the angle β can be computed using Equation 4:

$$\beta = 90 + (\varphi - \theta) \quad (\text{Eq 4})$$

If the forces are dominated mainly by the pressure forces, the difference between φ and θ will be small, and the angle β will be close to 90° . Deviations from 90° will indicate the presence of viscous forces acting on the blade.

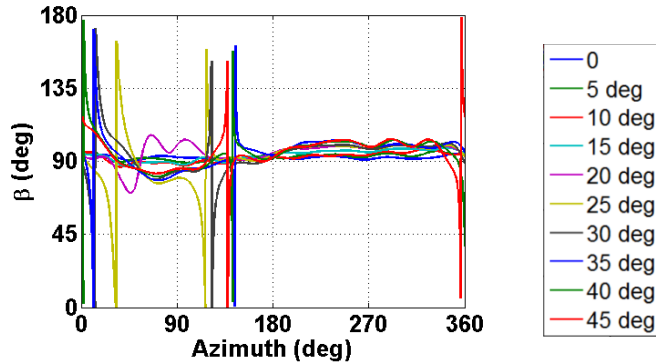


Fig. 27: β versus azimuth for $\pm 0^\circ$ to $\pm 45^\circ$ dynamic pitching.

Figure 27 shows the variation of β as a function of the azimuth for all of the dynamic pitching amplitudes. As seen from the figure, for all of the amplitudes, the angle remains close to 90° , which confirms the domineering role of pressure forces as opposed to the shear viscous forces acting parallel to the blade. This is a significant finding considering the ultra-low Reynolds numbers the blade is operating where viscous forces are relatively large.

STATIC VERSUS DYNAMIC PITCHING

Since there are significant differences in the lift and drag coefficients between the static and dynamic pitching cases, it is important to compare the flowfield for the two cases at the

exact same pitch angles to understand the key reason for the lift enhancement for the dynamic case. Figure 28 shows a comparison of PIV measured velocity vectors and vorticity contours for static and dynamic pitching cases. The static pitch angles include 15° , 30° , and 45° , and the dynamic cases include $\pm 15^\circ$, $\pm 30^\circ$, and $\pm 45^\circ$. For the dynamic pitch case, flowfield at the azimuthal location of 90° is compared because that is where the blade pitch angle reaches $+15^\circ$, $+30^\circ$, and $+45^\circ$, respectively for the three cases. Therefore, in this comparative study the flowfields are compared at the same pitch angle, but one subjected to steady flow and the other to unsteady flow conditions.

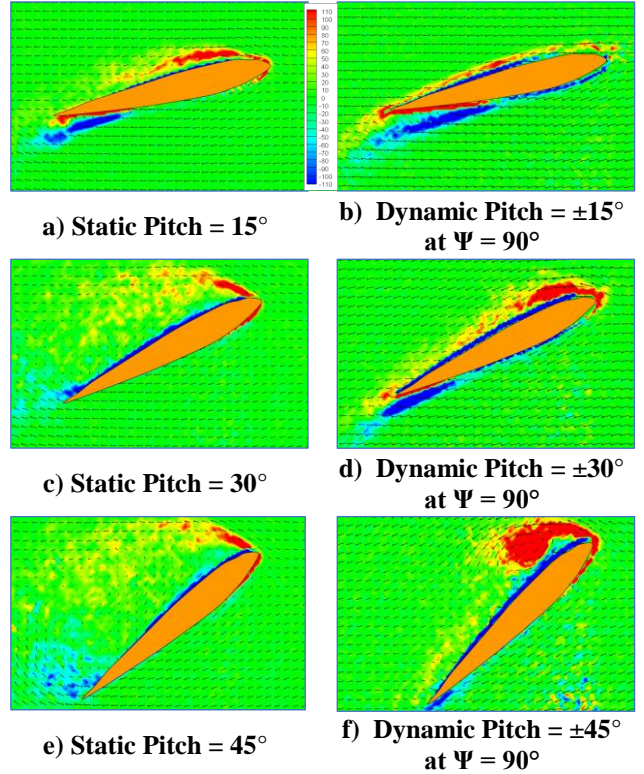


Fig. 28: Static versus dynamic PIV comparison for 15° , 30° , and 45° pitch angles.

In Figs. 28 (a) and (b) the blade is at a low angle of attack of 15° ; even then, for the static case, as seen from Fig. 28 (a), the flow has already separated from the leading edge and re-attaches close to the trailing edge forming a large laminar separation bubble (LSB), which is typical on steady airfoil at very low Reynolds numbers. However, for the dynamic case shown in Fig. 28 (b), when the blade reaches $+15^\circ$ angle of attack the flow is still fully attached showing no signs of stall. The static and dynamic cases for the 30° pitch angle is compared in Figs. 28 (c) and (d), respectively. For the 30° static case (Fig. 28 (c)), as expected, the flow is fully separated from the leading edge denoting deep stall; however, for the dynamic case (Fig. 28 (d)), at the same pitch angle of 30° , one can see the initiation of the dynamic stall vortex and the flow is still more or less attached. For the 45° static case shown in Fig. 28 (e), the flow is fully separated from the leading edge. However, for the dynamic case (Fig. 28 (f)), the

dynamic stall vortex has reached the full strength and is in the process of shedding. Comparing Fig. 28 (b), (d) and (f) would provide insight into how the pitching amplitude affects the dynamic stall process on a cyclorotor blade at ultra-low Reynolds numbers. These PIV results clearly explain the reason for the large lift coefficients measured on a dynamic pitching blade at high amplitudes (Figs. 19 and 23).

UNDERSTANDING PHYSICS OF FORCE PRODUCTION ON CYCLOROTOR BLADE

The variation of lift and drag coefficients as a function of azimuth on a blade operating at $\pm 30^\circ$ pitch amplitude is shown in Figs. 29 and 30. As mentioned before the lift is the force in the radial direction (positive lift is radially outward) and drag is the force in the tangential direction (positive drag is opposite to the direction of blade motion). Fig. 31 shows the measured flowfield around the azimuth (Ψ) at a 10° resolution. On Figs. 29 and 30 the corresponding PIV figure numbers (Figs. 31 (i) – (xxxvi)) are provided at a resolution of 10° . Also, to improve clarity in the discussion, each of the flowfield images include the lift vector where the magnitude is proportional to the measured magnitude (Fig. 29 and 30) and the direction depends on the sign. Similar to what is shown in Fig. 16, the computed virtual camber chord-line is superimposed on the physical airfoil in Fig. 31 to aid in the explanation of the physics.

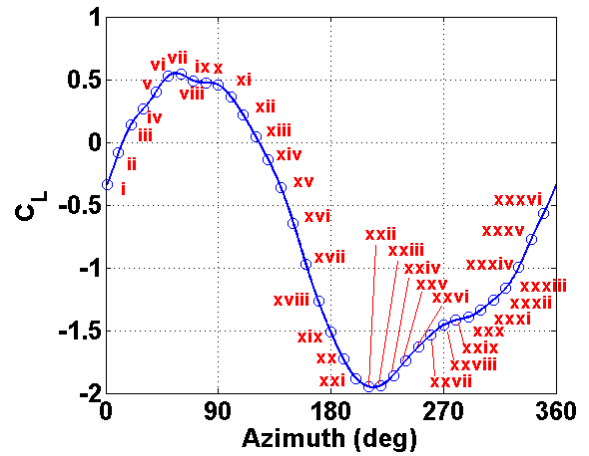


Fig. 29: Measured lift coefficient versus azimuth for $\pm 30^\circ$ dynamic pitching.

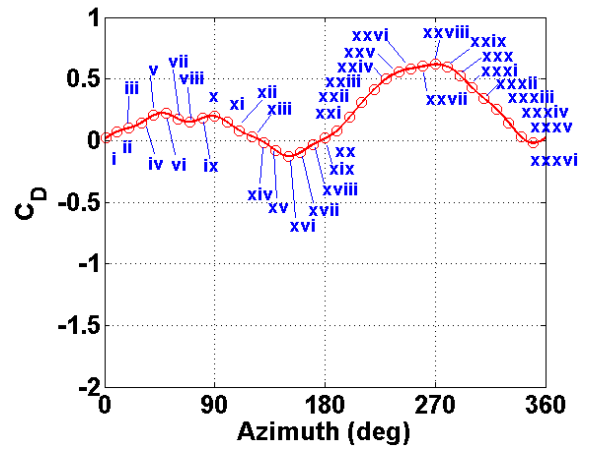
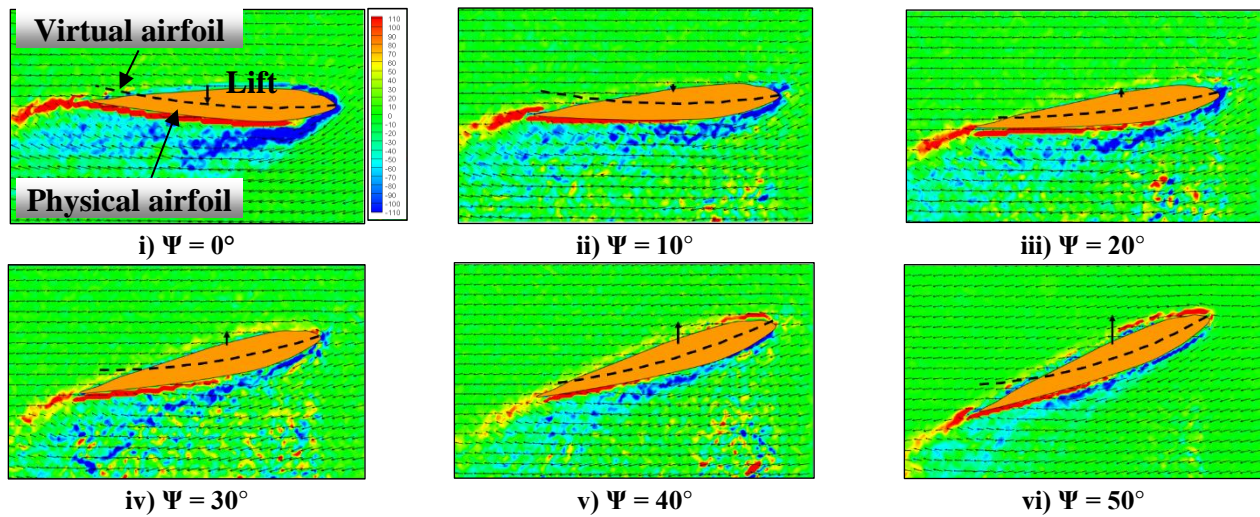
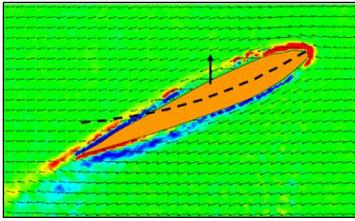
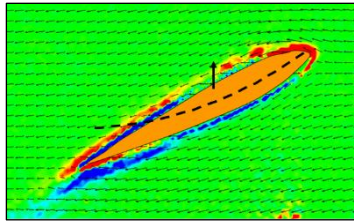


Fig. 30: Measured drag coefficient versus azimuth for $\pm 30^\circ$ dynamic pitching.

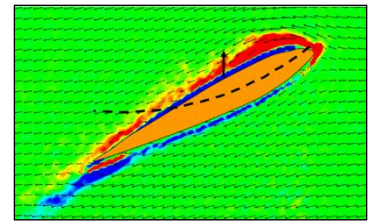




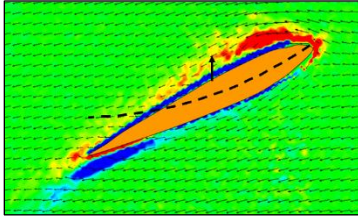
vii) $\Psi = 60^\circ$



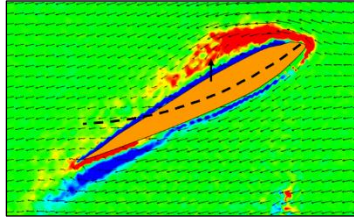
viii) $\Psi = 70^\circ$



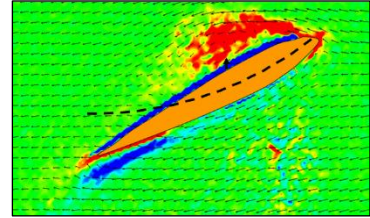
ix) $\Psi = 80^\circ$



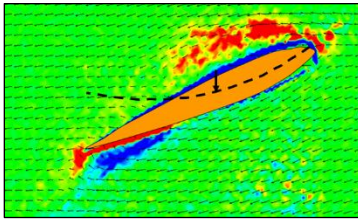
x) $\Psi = 90^\circ$



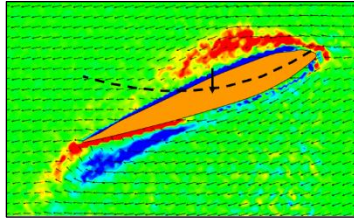
xi) $\Psi = 100^\circ$



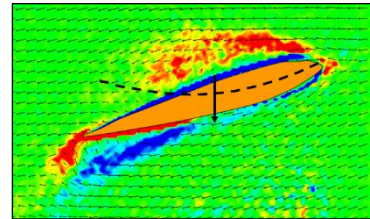
xii) $\Psi = 110^\circ$



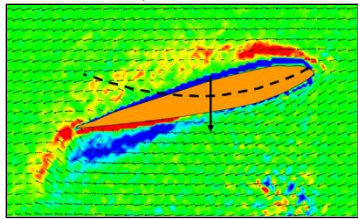
xiii) $\Psi = 120^\circ$



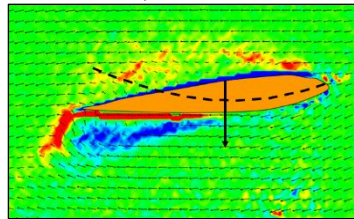
xiv) $\Psi = 130^\circ$



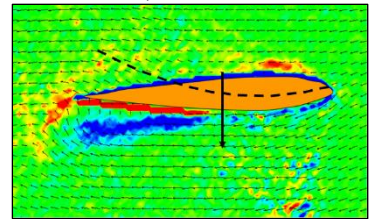
xv) $\Psi = 140^\circ$



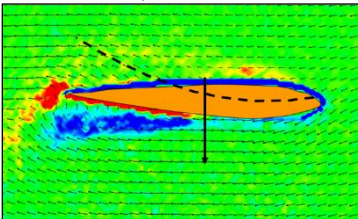
xvi) $\Psi = 150^\circ$



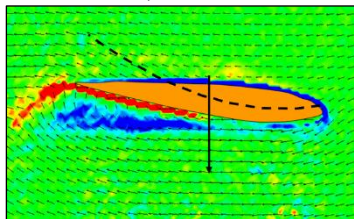
xvii) $\Psi = 160^\circ$



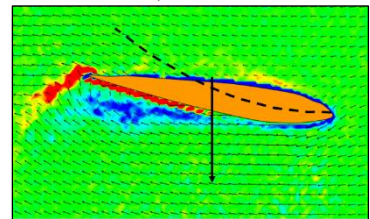
xviii) $\Psi = 170^\circ$



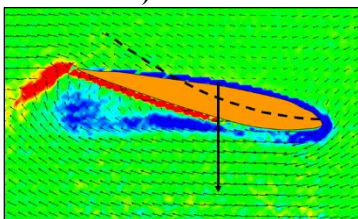
xix) $\Psi = 180^\circ$



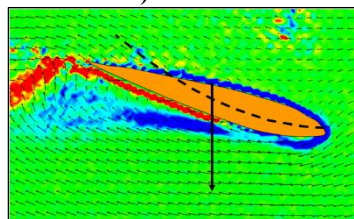
xx) $\Psi = 190^\circ$



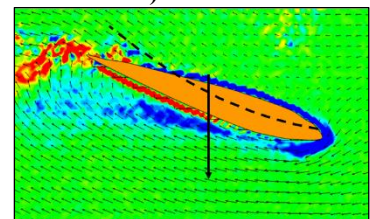
xxi) $\Psi = 200^\circ$



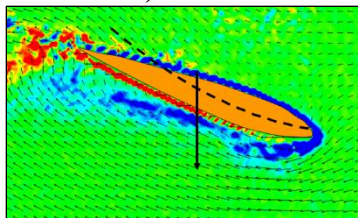
xxii) $\Psi = 210^\circ$



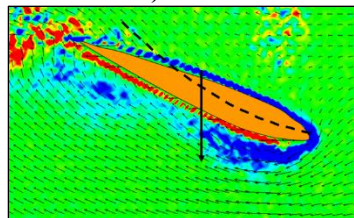
xxiii) $\Psi = 220^\circ$



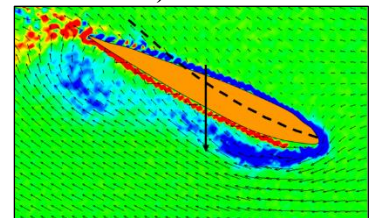
xxiv) $\Psi = 230^\circ$



xxv) $\Psi = 240^\circ$



xxvi) $\Psi = 250^\circ$



xxvii) $\Psi = 260^\circ$

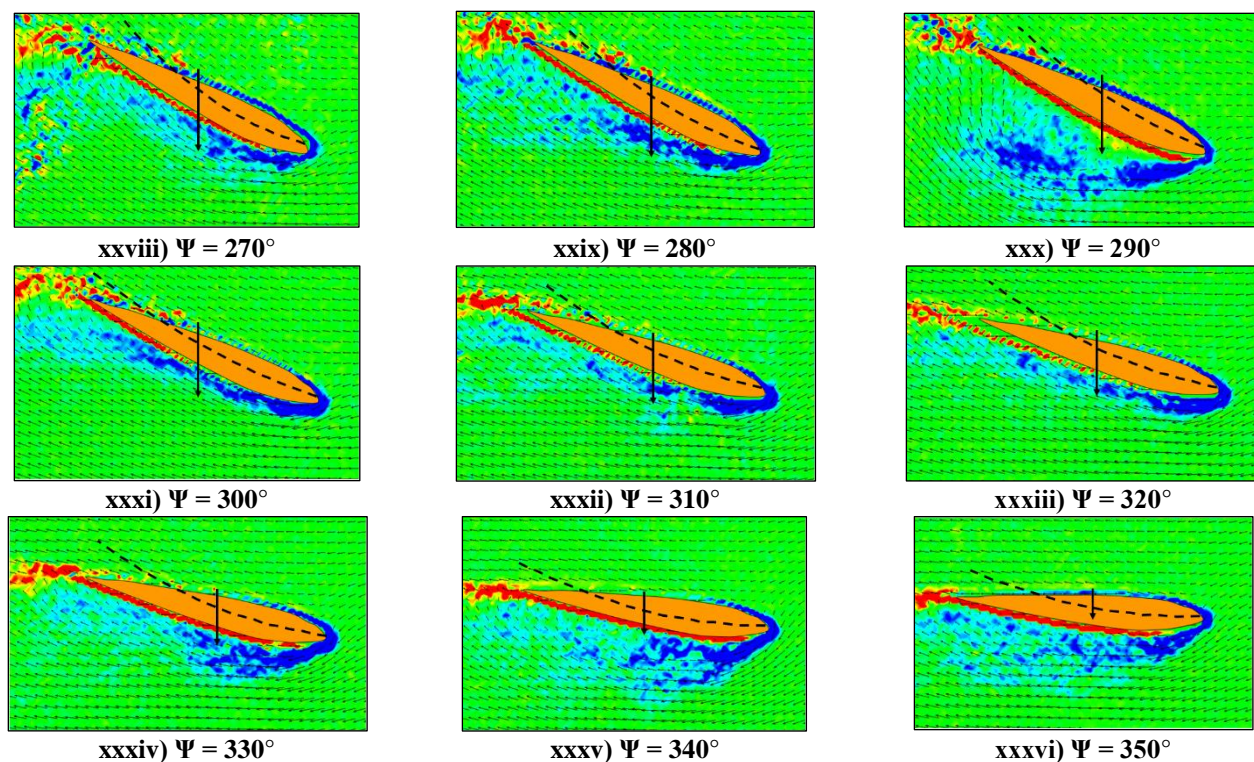


Fig. 31: PIV measured flow velocity vectors and vorticity contours at different azimuthal locations for $\pm 30^\circ$ dynamic pitching.

At 0° azimuth (Fig. 31 (i)), even though the airfoil is symmetric and pitch is zero, the small negative virtual camber shown in the figure creates a small negative lift. This can also be seen in Fig. 29. The direction of lift is also very evident from the flowfield around the airfoil. As seen from Fig. 30, the drag is very small and positive. In Fig. 31 (ii), since the pitch is increasing in the positive direction, the negative lift is decreasing. It is interesting because the lift is downwards or negative due to the virtual camber as shown in the figure. In other words, here the virtual camber is in the reverse direction of the conventional camber and hence it will be called ‘negative camber’. Typically, because of the positive pitch angle, the lift should be upwards or positive. However, in Fig. 31 (ii), the negative camber effect is more dominating than the effect of positive pitch angle and hence results in a negative lift. Again, as before, the direction of lift is evident from the flowfield as well. The drag increases due to the increase in pitch angle (Fig. 30).

At the 20° azimuth location (Fig. 31 (iii)), the pitch angle has increased further and the lift is close to zero because the negative lift from negative virtual camber is nullified by positive pitch. This could be thought of as the zero-lift angle of attack for the virtually cambered airfoil. It is important to note that, as shown in Figs. 13 (a) and 16, the camber of the virtual airfoil changes from one azimuthal location to another. At 30° azimuth (Fig. 31 (iv)), the blade pitch is further increased and now positive lift is generated, which means the pitch is high enough to dominate negative virtual camber. As shown in Fig. 31 (v), the lift increases for the 40° azimuth

because of the increase in blade pitch angle. At 50° azimuth (Fig. 29, 30 and Fig. 31 (vi)), both lift and drag reach a local maximum value. The blade camber has also increased significantly from the 0° azimuth.

Starting at 60° azimuth, the lift starts dropping even though the pitch angle is increasing. This may be because of the large increase in negative virtual camber and negative virtual incidence, which is reducing the effective angle of attack and the lift produced. However, more prominent than the drop in lift is the sudden local drop in drag. The reason for this can be traced back to the flowfield shown in Fig. 31 (vii), which shows the initiation of a vortex at the leading edge causing leading edge suction, which could reduce the net profile drag. Lift further decreases for the 70° azimuth (Fig. 31 (viii)) even though the pitch is increasing. Again, this occurs because of the large negative virtual camber and incidence from the reduced pitch rate. Drag drops further because of the increased leading edge suction as seen from the vorticity contours in the flowfield. From the 70° to 80° azimuth (Fig. 31 (ix)), the lift stays almost constant (refer to Fig. 29). However, from the flowfield, a strong dynamic stall vortex can be seen. At this point it is unclear why the vortex lift does not significantly increase the blade lift (Fig. 29). However, there is a slight increase in drag (Fig. 30). At the 90° azimuthal location (Fig. 31 (x)), the blade reaches its maximum pitch angle. At this point, there is significant negative virtual camber and incidence, as well as a strong dynamic stall vortex forming on the leading edge. The flow remains more or less attached on the top even at such high pitch angles. The lift

drops slightly, possibly due to the negative camber and incidence that is more effective than the additional vortex lift.

In Figures 31 (xi) – (xv), the 100° to 140° azimuthal locations show the shedding of the dynamic stall vortex and a reduction in the lift and drag (Figs. 29 and 30). It is also significant to note the large negative virtual camber and incidence for these cases. From the 110° to 120° azimuth, the direction of lift and drag changes from positive to negative (refer Figs. 29, 30, 31 (xii) and 31 (xiii)). This is because the negative virtual camber and incidence have increased to such an extent that it dominates even large positive pitch angles. This clearly shows the strong effect of dynamic virtual camber on the force production of a cyclorotor blade. Interestingly the drag (tangential force) becomes negative, indicating power extraction from the 115° to 170° azimuthal locations.

From 150° (Fig. 31 (xvi)) to 180° (Fig. 31 (xix)), there is large negative lift, which continues to increase due to the strong negative virtual camber. As seen from Figs. 13 (a), 16 and 31 (xix), the maximum virtual camber occurs at the 180° azimuth, causing a huge negative lift force, even with a symmetric airfoil and physical pitch angle of zero. Again, the direction of lift is evident from the flowfield. The drag also increases as shown in Fig. 30. At the 190° azimuth, as seen from Fig. 31 (xx), the camber is consistent with the blade pitch angle and is called ‘positive camber’. In the entire lower half (180° to 360°) the camber will not oppose the pitch angle, which is the case in the upper half (0° to 180°). In the entire lower half, the lift will be negative because it will be acting radially inwards towards the center of the rotor. From the 190° to 220° azimuthal locations (Figs. 29, 31 (xx) – (xxiii)) the magnitude of negative lift keeps increasing due to the positive camber. Also, from the flowfield, a strong trailing edge separation can be seen, which increases with increasing pitch angle.

From the 220° to 270° azimuth, the magnitude of negative lift starts decreasing but the drag coefficient keeps increasing until it reaches a maximum value of 0.6 at the 270° azimuth. At this position the blade attains the maximum pitch angle. The 230° azimuth (Fig. 31 (xxiv)) shows a weak dynamic stall vortex beginning to appear on the leading edge. It is weaker in nature mostly because virtual camber is positive and hence decreases flow separation (unlike the upper half where the camber was negative or reverse camber).

For azimuths of 240° – 260° (Figs. 31 (xxv) – (xxvii)) the dynamic stall vortex builds up strength. There is a mild shedding at approximately 270° (Fig. 31 (xxviii)). The vortex is fully separated at the 290° azimuth (Fig. 31 (xxx)). During this time, the magnitude of effective angle of attack is very high causing large lift and drag. It is also important to note that even though the pitching is symmetric, the dynamic stall process in the upper and lower half of the circular trajectory is completely different because of the complete reversal of dynamic virtual camber from the upper to lower half. From the 300° to 320° azimuth (Fig. 31 (xxxi) – (xxxiii)), the flow again starts re-attaching as pitch decreases. The magnitude of lift and drag decreases as seen from Figs. 29 and 30. However,

from the 330° to 350° azimuth (Figs. 31 (xxxiv) – (xxxvi)), the shedding of a secondary leading edge vortex can be seen. The reason for this is not completely understood at this point. Finally, at 360° (Fig. 31 (i)), the flow reattaches again.

A key insight gained from these measurements is the interplay of blade pitch angle and dynamic virtual camber in the blade force production. In the entire upper half, the pitch angle and virtual camber oppose each other, unlike the lower half where they act in the same direction. This leads to completely different dynamic stall process in the upper and lower halves. This can also explain why a huge improvement in cyclorotor performance is obtained using asymmetric blade pitching (Ref. 6), where the pitch angle in the upper half increased and decreased in the lower half.

POWER CALCULATIONS

Also of interest is the power consumption of a dynamic pitching cyclorotor blade. Figure 32 shows the measured instantaneous blade power breakdown for the $\pm 45^\circ$ dynamic pitching case as a function of azimuth. Included in the plot are the power required for the blade to rotate, the power required for the blade to pitch, and the total power. These are calculated using the following equations:

$$\text{Rotation power } (P_{ROT}) = D\Omega R \quad (\text{Eq } 5)$$

$$\text{Pitching power } (P_{PITCH}) = M_Z \dot{\theta} \quad (\text{Eq } 6)$$

$$\text{Total power} = P_{ROT} + P_{PITCH} \quad (\text{Eq } 7)$$

where D is the measured tangential force, which is referred to as the drag force in this paper, ΩR is the rotational velocity, M_Z is the measured pitching moment, and $\dot{\theta}$ is the measured pitch rate.

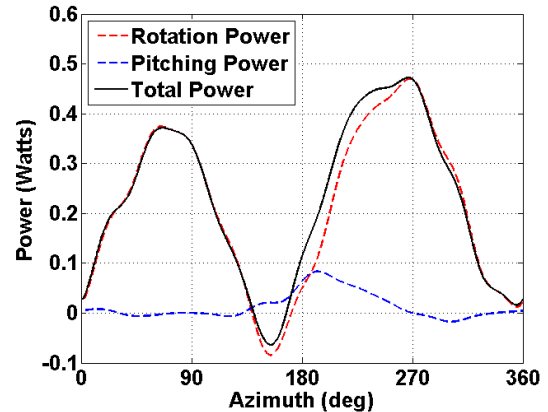


Fig. 32: Measured blade power versus azimuth for $\pm 45^\circ$ pitching.

It is clear from Fig. 32 that most of the power is required for the blade rotation and not pitching. The present study conclusively proves that it only takes up a very small fraction of the total aerodynamic power to dynamically pitch the blades at least at such low Reynolds numbers. Figure 33 shows the instantaneous total blade power versus the azimuth for all of the dynamic pitching cases. It can be seen that, as expected, the power continues to increase as the dynamic pitching amplitude increases. In fact for a small part of the

azimuthal cycle the blade power is negative or blade is extracting power.

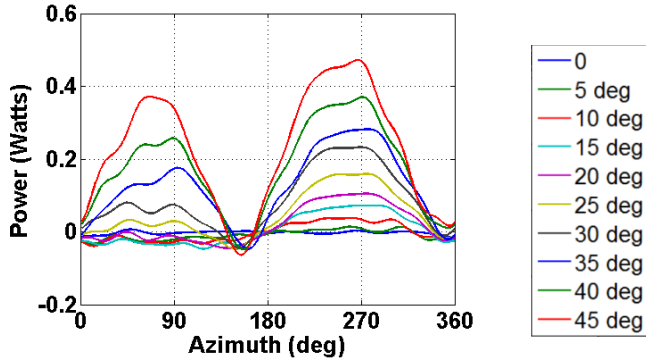


Fig. 33: Measured blade power versus azimuth for $\pm 0^\circ$ to $\pm 45^\circ$ dynamic pitching.

The cycle-averaged power versus the pitching amplitude for all the dynamic pitching cases is plotted in Fig. 34. As seen from the figure, the power increases quadratically with the pitching amplitude. For the pitching amplitudes of 5° and 10° the power is slightly negative denoting power extraction or negative induced power in a cycle-averaged sense. Similarly, for 0° , the average power is close to zero may be because the component of lift vector in the forward direction (causing negative induced power) cancels out the profile power. From 20° to 45° the power increases rapidly until it reaches a maximum of about 0.24 Watts.

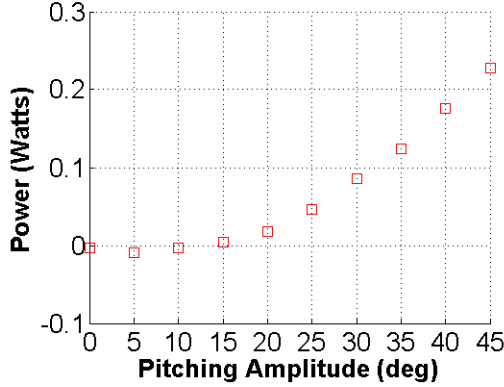


Fig. 34: Cycle-averaged blade power versus blade pitching amplitude.

In Figure 35 the cycle-averaged thrust is plotted against the dynamic pitching amplitude. The cycle-averaged thrust (T) is computed as follows:

$$T = \sqrt{F_z^2 + F_y^2} \quad (\text{Eq 8})$$

Where F_z and F_y are vertical and horizontal components (in the fixed frame, refer Fig. 2) of measured radial and tangential forces. As seen from the figure, there is a nonlinear relationship between the average thrust produced by the rotor and the dynamic pitching amplitude.

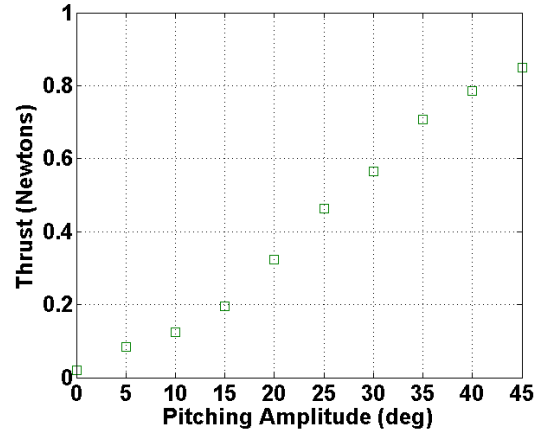


Fig. 35: Cycle-averaged thrust versus blade pitching amplitude.

Figure 36 has the cycle-averaged thrust to power ratio as a function of pitching amplitudes of 25° to 45° . It can be seen that the power loading decreases with respect to the pitching amplitude. The unusually high power loading values can be attributed to extremely low disk loading at which the present rotor is operating. For the 45° pitching amplitude, based on the rectangular projected area of the rotor, the disk loading is around 16 N/m^2 (0.33 lb/ft^2), which is extremely low.

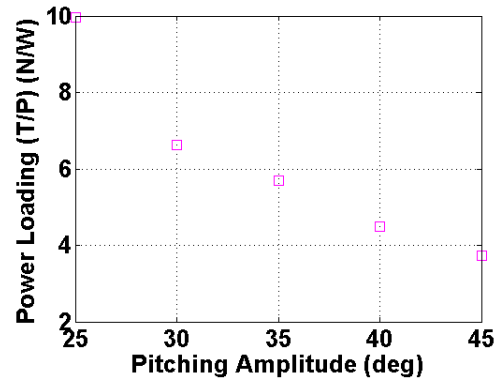


Fig. 36: Cycle-averaged power loading (T/P) versus blade pitching amplitude.

The decrease in power loading with pitch amplitude can be attributed to the fact that the disk loading is increasing and the figure of merit is decreasing with pitch amplitude. The figure of merit (FM) is defined as following:

$$FM = \frac{P_{IDEAL}}{P_{MEASURED}} \quad (\text{Eq 9})$$

P_{IDEAL} , the ideal power, is given as:

$$P_{IDEAL} = T v_i \quad (\text{Eq 10})$$

where v_i , the induced velocity calculated as follows:

$$v_i = \sqrt{\frac{T}{2\rho A}} \quad (\text{Eq 11})$$

where ρ is the density of water and A is the rectangular projected area of the rotor ($A = b \times d$), where b is the blade span and d is the cyclorotor diameter.

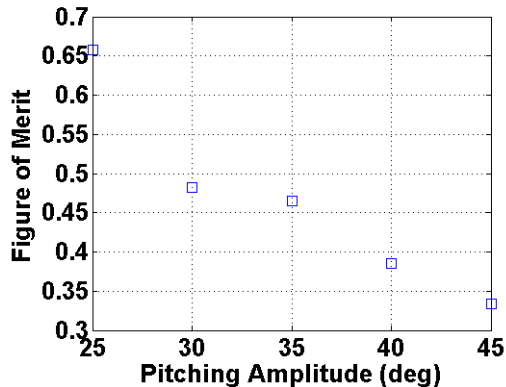


Fig. 37: Figure of merit versus blade pitching amplitude.

The figure of merit is plotted a function of pitch amplitude in Fig. 37. It can be seen that FM drops with pitch amplitude; however, for a pitch amplitude of $\pm 25^\circ$, the FM is around 0.65, which is very high considering the ultra-low Reynolds numbers ($Re \sim 18,000$) at which the blade is operating. However, as seen from Fig. 37, for a pitch amplitude of $\pm 45^\circ$, the FM is around 0.34. This decrease in FM is mainly due to the higher drag coefficient (Fig. 24) which the blade experiences at larger blade pitching angles.

CONCLUSIONS

The present study provides an in-depth understanding of the unsteady aerodynamic mechanisms on a cyclorotor blade operating at ultra-low Reynolds numbers ($Re \sim 18,000$). This is accomplished by utilizing a combination of force and flowfield measurements in conjunction with CFD simulations. This is the first time the instantaneous blade fluid dynamic forces on a cyclorotor blade were measured, which, along with PIV-based high resolution flowfield measurements around the blade at different azimuthal locations, revealed the key fluid dynamic mechanisms acting on the blade. A 2D CFD analysis of the cycloidal rotor was developed, which correlated well with experiments for both the force and flowfield. Studies were performed with both static and dynamic blade pitching. Direct comparison of the static and dynamic pitch experimental results helped isolate the unsteady aerodynamic phenomena from the steady effects.

Specific conclusions from this study are as follows:

1. Large dynamic virtual camber induced by the inherent flow curvature and blade pitch rate caused asymmetry in lift and drag coefficients between positive and negative pitch for both the static and dynamic pitching cases.
2. The unsteady blade force coefficients were almost double the static ones clearly indicating the role of

unsteady aerodynamic mechanisms on the force production on cyclorotor blades. This explains the ability of a cyclorotor to produce large thrust at relatively lower rotational speeds, which was a key inference from the previous performance studies.

3. For the dynamic case, the blade lift coefficient monotonically increased even up to $\pm 45^\circ$ pitch amplitude due to dynamic stall phenomenon, which kept the flow attached until higher pitch angles. On the other hand, for the static case, the flow separated from the leading edge after around 15° with a large laminar separation bubble (LSB) and eventually completely separating at higher pitch angles.
4. The CFD flow solution and PIV measured flowfield correlated very well and both showed the formation and shedding of strong leading edge or dynamic stall vortices, especially at higher pitch amplitudes, which is the reason for the stall delay and force enhancement.
5. Dynamic stall processes in the upper and lower halves of the circular blade trajectory were completely different because of the reversal of the virtual blade camber from upper to lower half.
6. The measured resultant forces were mostly normal to the chord for the dynamic pitch cases indicating that the pressure force, as opposed to viscous force, is dominant on a cyclorotor blade (even at these ultra-low Reynolds numbers).
7. The power required for blade rotation (rather than pitching power) is the significant component of the total power required for dynamic pitching cyclorotor blade.
8. The cyclorotor figure of merit (FM) drops at higher pitch amplitudes due to higher dynamic drag coefficients.

ACKNOWLEDGEMENTS

This research was supported by the U.S. Army's Micro Autonomous Systems and Technology-Collaborative Technology Alliance (MAST-CTA) with Chris Kroninger and Brett Piekarski (Vehicle Technology Directorate, Army Research Laboratory) as Technical Monitors. The authors would also like to thank undergraduate student Farid Saemi for his contributions to the experimental setup.

REFERENCES

- ¹Pines and Bohorquez, "Challenges Facing Future Micro-Air Vehicle Development," *Journal of Aircraft*, Vol. 43, No. 2, April 2006, pp. 290-305.
- ²Hein, B., and Chopra, I., "Hover Performance of a Micro Air Vehicle: Rotors at Low Reynolds Number," *Journal of American Helicopter Society*, Vol. 52, No. 3, July 2007, pp. 254-262.

- ³Benedict, M., “Fundamental Understanding of the Cycloidal-Rotor Concept for Micro Air Vehicle Applications,” Ph.D Thesis, Department of Aerospace Engineering, University of Maryland College Park, December 2010.
- ⁴Benedict, M., Ramasamy, M., Chopra, I., and Leishman, J. G., “Performance of a Cycloidal Rotor Concept for Micro Air Vehicle Applications,” *Journal of the American Helicopter Society*, Vol. 55, No. 2, April 2010, pp. 022002-1 - 022002-14.
- ⁵Benedict, M., Ramasamy, M., and Chopra, I., “Improving the Aerodynamic Performance of Micro-Air-Vehicle-Scale Cycloidal Rotor: An Experimental Approach,” *Journal of Aircraft*, Vol. 47, No. 4, July-August 2010, pp. 1117 – 1125.
- ⁶Benedict, M., Jarugumilli, T., and Chopra, I., “Experimental Optimization of MAV-Scale Cycloidal Rotor Performance,” *Journal of the American Helicopter Society*, Vol.56, No.2, April2011, pp.022005-1 -022005-11.
- ⁷Benedict, M., Jarugumilli, T., and Chopra, I., “Effect of Rotor Geometry and Blade Kinematics on Cycloidal Rotor Hover Performance,” *Journal of Aircraft*, Vol. 50, No. 5, 2013, pp. 1340 – 1352.
- ⁸Benedict, M., Jarugumilli, T., Lakshminarayan, V. K., and Chopra, I., “Effect of Flow Curvature on the Forward Flight Performance of a MAV-Scale Cycloidal Rotor,” *AIAA Journal*, Vol. 52, No. 6, 2014, pp. 1159 – 1169.
- ⁹Lind, A. H., Jarugumilli, T., Benedict, M., Lakshminarayan, V. K., Jones, A. R., and Chopra, I., “Flowfield studies on a micro-air-vehicle-scale cycloidal rotor in forward flight,” *Experiments in Fluids*, Vol. 55, November 2014, pp. 1 – 17.
- ¹⁰Jarugumilli, T., Benedict, M., and Chopra, I., “Wind Tunnel Studies on a Micro Air Vehicle-Scale Cycloidal Rotor,” *Journal of the American Helicopter Society*, Vol. 59, No. 2, April 2014, pp. 1 – 10.
- ¹¹Benedict, M., Mattaboni, M., Chopra, I., and Masarati, P., “Aeroelastic Analysis of a Micro-Air-Vehicle-Scale Cycloidal Rotor in Hover,” *AIAA Journal*, Vol. 49, No. 11, November 2011, pp. 2430 – 2443.
- ¹²Benedict, M., Gupta, R., and Chopra, I., “Design, Development and Flight Testing of a Twin-Rotor Cyclocopter Micro Air Vehicle,” *Journal of the American Helicopter Society*, Vol. 58, No. 4, October 2013, pp. 1 – 10.
- ¹³Elena, S., Hrishikeshavan, V., Benedict, M., Yeo, D., and Chopra, I., “Development of Control Strategies and Flight Testing of a Twin-Cyclocopter in Forward Flight,” Proceedings of the 70th Annual National Forum of the American Helicopter Society, Montreal, Quebec, Canada, May 20–22, 2014.
- ¹⁴Benedict, M., Mullins, J., Hrishikeshavan, V., and Chopra, I., “Development of a Quad Cycloidal-Rotor Unmanned Aerial Vehicle,” *Journal of the American Helicopter Society*, Vol. 61, No. 2, April 2016, pp. 1 – 12.
- ¹⁵Zachary, H., A., Benedict, M., Hrishikeshavan, V., and Chopra, I., “Design, Development, and Flight Test of a Small-Scale Cyclogyro UAV Utilizing a Novel Cam-Based Passive Blade Pitching Mechanism,” *International Journal of Micro Air Vehicles*, Vol. 5, No. 2, June 2013, pp. 145 – 162.
- ¹⁶Lakshminarayan, V. K., “Computational Investigation of Microscale Coaxial Rotor Aerodynamics in Hover,” Ph.D. Thesis, Department of Aerospace Engineering, University of Maryland College Park, 2009.
- ¹⁷Pulliam, T., Chaussee, D., “A Diagonal Form of an Implicit Approximate Factorization Algorithm,” *Journal of Computational Physics*, Vol. 39, No. 2, 1981, pp. 347–363.
- ¹⁸Van Leer, B., “Towards the Ultimate Conservative Difference Scheme V. A Second-Order Sequel to Godunov’s Method,” *Journal of Computational Physics*, Vol. 135, No. 2, 1997, pp. 229–248.
- ¹⁹Roe, P., “Approximate Riemann Solvers, Parameter Vectors and Difference Schemes,” *Journal of Computational Physics*, Vol. 135, No. 2, 1997, pp. 250–258.
- ²⁰Koren, B., “Multigrid and Defect Correction for the Steady Navier–Stokes Equations”, Proceedings of the 11th International Conference on Numerical Methods in Fluid Dynamics, Williamsburg, VA, June 1988.
- ²¹Turkel, E., “Preconditioning Techniques in Computational Fluid Dynamics,” *Annual Review of Fluid Mechanics*, Vol. 31, 1999, pp. 385–416.
- ²²Spalart, P.R., Allmaras, S.R. “A One-equation Turbulence Model for Aerodynamics Flows,” Proceedings of the 30th AIAA Aerospace Sciences Meeting and Exhibit, Reno, NV, January 6–9, 1992.
- ²³Halder, A., Walther, C., and Benedict, M., “Unsteady Hydrodynamic Modeling of Cycloidal Propeller,” To appear in the Proceedings of the Fifth International Symposium on Marine Propulsors, Helsinki, Finland, June 12 –15, 2017.